

## Research Article

# Influence of Surface Roughness on a Highly Loaded Axial Compressor Stage Performance at Low Reynolds Number

Hongzhi Cheng <sup>1,2,3</sup> Mingyang Wang,<sup>1,2,3</sup> Chuangxin Zhou,<sup>1,2,3</sup> Shengfeng Zhao <sup>1,2,3</sup>  
Xingen Lu,<sup>1,2,3</sup> and Junqiang Zhu<sup>1,2,3</sup>

<sup>1</sup>Key Laboratory of Light-Duty Gas-Turbine, Institute of Engineering Thermo-Physics, Chinese Academy of Sciences, Beijing, China

<sup>2</sup>University of Chinese Academy of Sciences, Beijing, China

<sup>3</sup>Innovation Academy for Light-Duty Gas Turbine, Chinese Academy of Sciences, Beijing, China

Correspondence should be addressed to Shengfeng Zhao; zhaoshengfeng@iet.cn

Received 31 May 2021; Revised 20 August 2021; Accepted 13 September 2021; Published 23 October 2021

Academic Editor: Rosario Pecora

Copyright © 2021 Cheng Hongzhi et al. This is an open access article distributed under the Creative Commons Attribution License, which permits unrestricted use, distribution, and reproduction in any medium, provided the original work is properly cited.

In the present study, a numerical simulation was conducted to investigate the influence of surface roughness on the aerodynamic performance of a 1.5-stage highly loaded axial compressor at low Reynolds number. It was especially considered how the roughness Reynolds number ( $k^+$ ) affected the change of the inlet and outlet conditions, the growth of the separation bubble (LSB), the status of the limiting streamline, and the patterns of the wake. Regarding the roughness settings, five roughness magnitudes and four roughness locations were mainly studied. The results showed that at low Re, surface roughness mainly improved the stage performance by reducing the length and width of the LSB as well as the rotor tip vorticity, delaying the occurrence of three-dimensional flow separation and increasing the turbulence level near the wall. However, it also aggravated the incoordination between the subsequent stages to a certain extent, which limited further improvement of the overall aerodynamic performance. Generally, with  $k^+$  increasing, the compressor aerodynamic performance improved and achieved the best at  $k^+ = 137.8$ . The maximum increases in the total pressure ratio, peak efficiency, and choked mass flow were approximately 4.01%, 5.34%, and 2.24%, respectively. In addition, for all the four roughness locations, the roughness covering from the leading edge to 50% of the axial chord length on the suction surface had a relatively evident advantage in improving the compressor peak efficiency because of the better control of the LSB and wall shear stress.

## 1. Introduction

When an unmanned aerial vehicle (UAV) cruises at high altitudes, the Reynolds number (Re) based on the blade chord decreased sharply, which seriously affects the separation, transition, and other flow conditions of the compressor blade surface [1, 2]. At a low Reynolds number ( $Re < 105$ ), the onset of the boundary layer transition is delayed, and the laminar flow tends to separate, forming a free shear layer that undergoes a subsequent transition to turbulent flow [3]. As the Re further decreases, there is usually only laminar separation but no turbulent reattachment on the blade surface, which leads to a severe reduction in the efficiency and steady work range of a compressor [4].

In order to further investigate and analyze the phenomenon and mechanism of the flow separation and transition on the turbomachinery blade surface at low Reynolds number and to improve the aerodynamic characteristics, scholars have adopted several active or passive techniques, including utilizing a flexible membrane [5], blade surface layer suction [6], casing treatments [7], pulsed vortex generator jets [8, 9], and surface roughness control [10]. Compared with the methods above, the surface roughness control method has shown superiority in effectively controlling the development of the boundary layer without imposing extra complex geometric shapes on the blade. In the past few decades, the influence of blade surface roughness on the aerodynamic performance of a compressor has become a hot research

topic, and the flow control method based on roughness has tremendous application potential [11].

Research on the effects of surface roughness of compressor cascades started early and extensive experiments and numerical simulations have been conducted for detailed investigations of roughness effects. Back et al. [12] measured the profile loss and deviation angle of a certain low-speed compressor cascade under different degrees of roughness and found that both properties increased with increasing roughness. In addition, the results showed that the roughness of the suction surface leading edge was the dominant factor in leading to variations in cascade performance, while the pressure surface roughness had little influence. Kong et al. [13] reported that roughness promoted strong turbulent separation near the trailing edge compared to smooth blades, which resulted in increased flow losses and asymmetrical wakes along the circumferential direction. Gbadebo et al. [14] covered the stator suction surface with a sandpaper. The experiment revealed that the compressor performance significantly decreased when the rough surface was set between the leading edge and the peak velocity of the suction surface, while the influence could be ignored when the roughness was set downstream of the peak velocity. Im et al. [15] used the LDV technique to measure the boundary layer velocity and profile loss. The results indicated that the size of the separation bubble was inhibited at the leading edge and the turbulence level at the turbulent boundary layer decreased at  $Re = (2.1 \sim 3.8 \times 10^5)$ , leading to a reduction in the cascade profile loss.

For multistage axial compressors, much work has also been done to study the influences of surface roughness on the compressor stage performance. Syverud et al. [16, 17] obtained test results from a series of accelerated deterioration tests on a General Electric J85-13 jet engine compressor with eight stages to simulate the impact of surface roughness on compressor stage performance by spraying atomized salt-water into the engine intake. The surface roughness levels and applicable Reynolds numbers were found to increase profile losses, and the isentropic efficiency was reduced approximately three percentage points along the operating line. Morini et al. [18, 19] carried out numerical simulations to analyze the influence of dirt deposition and roughness level on the performance of NASA stage 37. The results showed that the decreased efficiency in the choked flow region mainly comes from the increase in flow blockage, while the roughness itself had little influence. Moreover, they proposed that stage performance was mainly affected by the roughness of the rotor compared with that of the stator, and the surface roughness of the suction side has a greater impact than that of the pressure side. Bammert and Woelk [20] took a three-stage axial flow compressor as the research object and compared the aerodynamic performance of blades with smooth and rough surfaces. The results reflected that the total pressure ratio was reduced by a maximum of 30% and that the volume flow rate was reduced by 15%-20% with roughness increasing. Chen et al. [21, 22] pointed out that increasing surface roughness had little effect on the stable working range of the compressor, while increasing blade thickness reduced the stable working range. Furthermore, their numerical calculation of stage 35 showed that

TABLE 1: Parameters of the 1.5-stage compressor.

Parameter	Design value
Design rotating speed (r/min)	25000
Total pressure ratio	1.72
Number of blades	31/36/59
Tip clearance (mm)	0.2
Hub clearance (mm)	0.15
Inlet chord length (mm)	23
Design tip speed (m/s)	361
Work coefficient	0.46
Inlet hub/tip radius ratio	0.72

the compressor performance dropped sharply when the roughness was located near the root of the rotor and that the roughness near the leading edge had a greater influence on the performance than the roughness near the trailing edge. In addition, the roughness of certain positions improved the compressor performance to a certain extent.

Despite the efforts highlighted above, previous research has mainly focused on high  $Re$  conditions. Under such conditions, surface roughness was likely to reduce peak efficiency and deteriorate compressor performance [23]. Thus far, a few studies focusing on low  $Re$  conditions have been carried out on large-scale cascades. However, few studies have been conducted on small-scale compressors, and the influence of the blade surface roughness on small compressors at low  $Re$  needs further study. Therefore, this paper presents a numerical simulation of a small-scale 1.5-stage highly loaded axial compressor under 20 km altitude conditions ( $Re = 4.5 \times 10^4$ ) to investigate in detail the influences of the local surface roughness of the rotor blade including roughness magnitudes and locations on the stage performance, as well as the aerodynamic parameter distributions and flow field characteristics.

## 2. Numerical Methods and Research Programs

**2.1. Baseline Geometry.** The compressor used in this study was a small-scale 1.5-stage highly loaded axial compressor, which was designed and tested by the laboratory of the Institute of Engineering Thermophysics, Chinese Academy of Sciences [24]. It was a typical axial compressor for small aeroengines. At the design point, the rotor operated at a speed of 25000 rpm. Detailed geometric and aerodynamic parameters are listed in Table 1.

### 2.2. Numerical Methods

**2.2.1. Flow Solver and Numerical Mesh.** Numerical simulations were performed using the commercial CFD software ANSYS CFX to study the effects of surface roughness on the compressor aerodynamic characteristics. The CFX code solves the 3D Reynolds-averaged form of the Navier-Stokes equations using the finite-element method based on a finite volume. Second-order upwind discretization in space and second-order central difference discretization in time are used. Furthermore, the code adopts 24-point interpolation

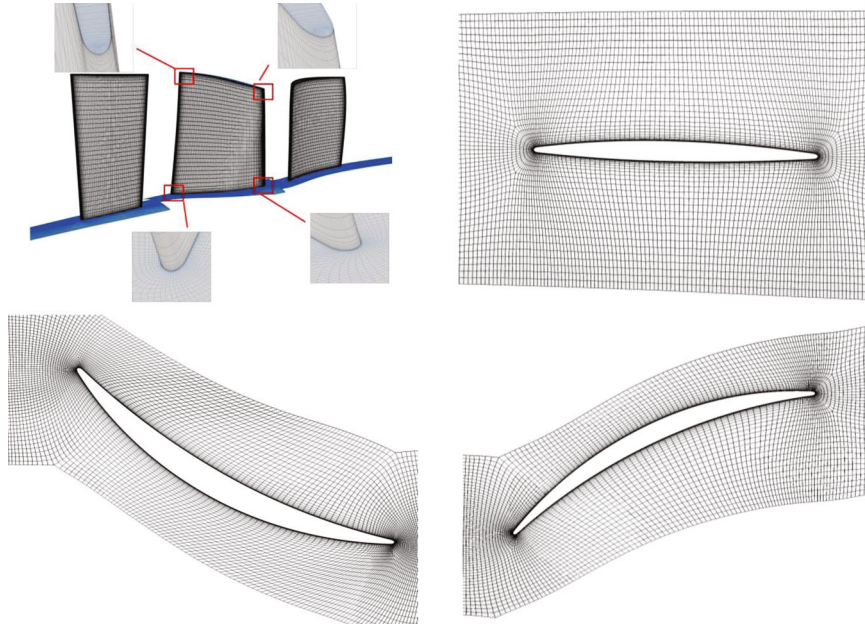


FIGURE 1: Computational grid structures in local domain of the compressor.

TABLE 2: Numerical parameters of the simulation at different altitudes.

Altitude/km	Total temperature At inlet (K)	Total pressure At inlet (Pa)	Physical rotation speed (r/min)	Corrected rotation speed	Reynolds number
0	288.15	101325	25000	100%	$5.5 \times 10^5$
20	216.65	5529.3	21678	100%	$4.5 \times 10^4$

for hexahedral mesh elements which take advantage of the numerical accuracy of the finite-element method, while ensuring the conservation characteristics of finite volume method.

The blade surface grid adopts the HOH topology structure, while the O4H topology structure is adopted at the blade root and tip clearance. To accurately capture the viscous flow near the wall, the solid wall at the blade surface and the shroud/hub were encrypted. A maximum dimensionless wall distance  $y^+ = 1$  was achieved on the first node from the solid wall, and the structured mesh was generated in NUMECA/Autogrid5 which was an automatic structured grid generator for turbine machinery based on template technology, dividing the o-type and H-type topology grids easily. Then the mesh was exported to the CFX solver for the next simulation. Structured meshing and block meshing techniques were used for the 1.5 stage compressor in this study. The numerical grid structures were shown in Figure 1.

The purpose of grid independence study was to find the smallest grid configuration and number that can reduce the amount of numerical calculation and ensure the accuracy of calculation. Moreover, the calculation result changed a little with the increase of the number of grids when achieving the grid independence. In this paper, five different numbers of grid configurations (1 million, 1.4 million, 1.8 million, 2.2 million, and 2.6 million) were selected, and the topological structures and the distance of the first mesh normal to the

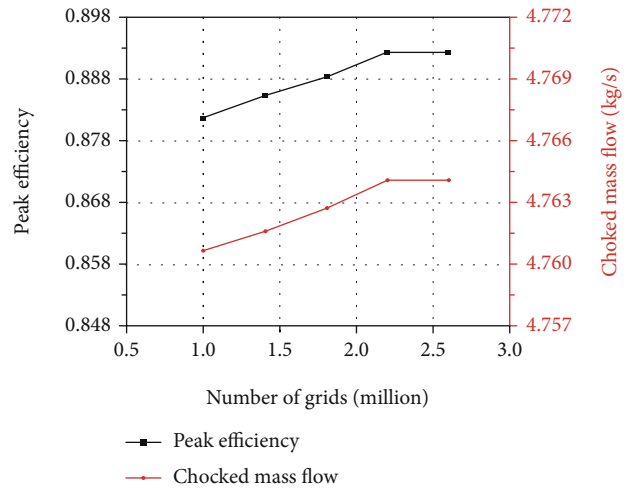


FIGURE 2: Grid independence validation.

end-wall (0.003 mm) of the five meshes were exactly the same. The shear stress transport (SST  $k-\omega$ ) turbulence model coupled with  $\gamma-\theta$  transition model was used for numerical verification (see below for comparison of turbulence models). Besides that, the boundary condition of the numerical validation part was set as the standard ground condition (0 km altitude), while that of low Re was set as 20 km altitude

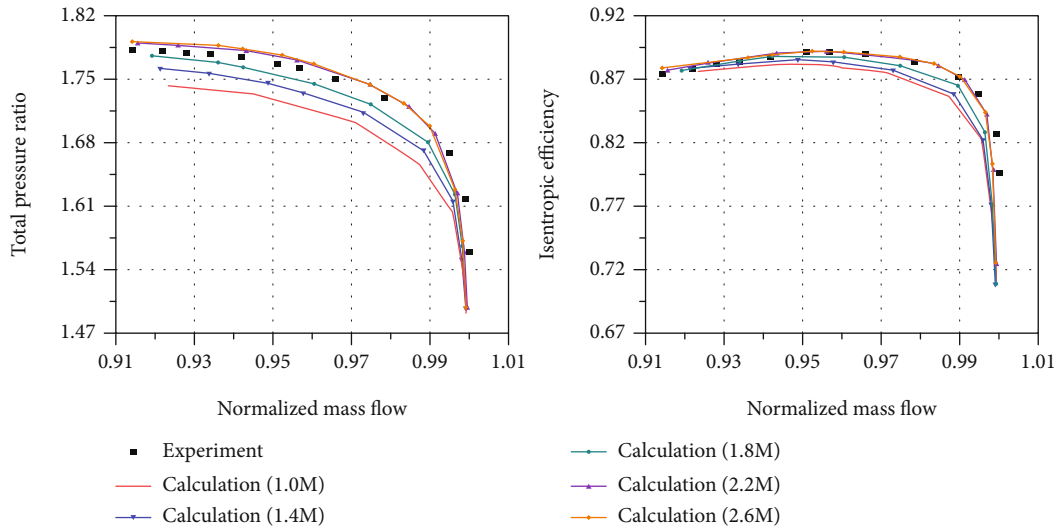


FIGURE 3: The calculation results of the five different meshes.

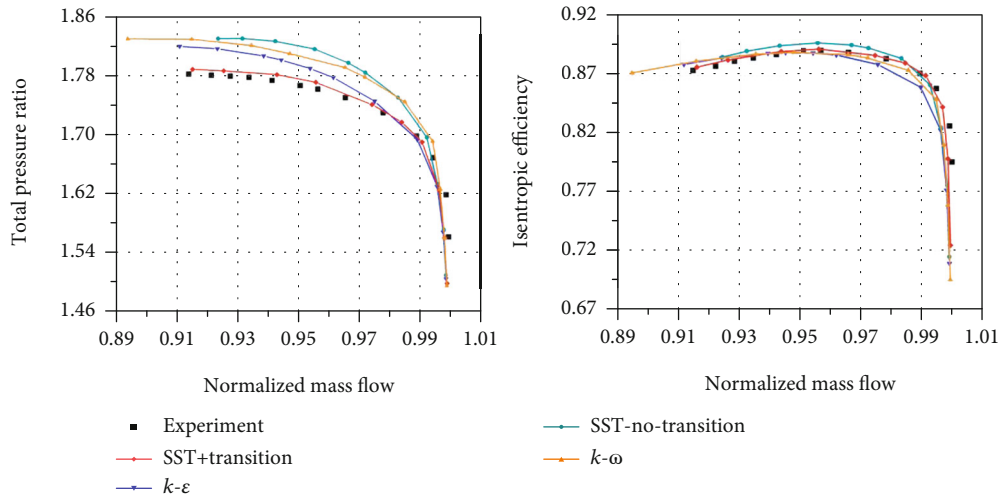


FIGURE 4: The compressor aerodynamic performance calculated by different turbulence models.

condition. Parameter settings are shown in Table 2, and specific boundary conditions are shown in the following section.

Figure 2 compares the choked mass flow and peak efficiency of the compressor calculated in different grids, and the results showed that the two performance parameters basically did not vary when the number of grid nodes reached 2.2 million. Furthermore, Figure 3 shows the total pressure ratio and isentropic efficiency curves of the compressor obtained by experiment and calculations (using the SST turbulence model coupled with  $\gamma$ - $\theta$  transition model for the five different meshes) at 100% design speed. As can be seen, the results changed a little as the number of grids increased from 2.2million to 2.6million, and the two calculated parameters of the compressor were in good agreement with the experimental results in the trend of the characteristic lines, with only slight differences in specific values. In general, for this compressor, it was considered that the grid

number of 2.2million had reached the requirement of grid independence, and this was used as the calculation grid of the further simulation.

#### 2.2.2. Boundary Condition Setting at Low Reynolds Number.

Total pressure  $P_0^1$  and total temperature  $T_0^1$  were fixed to an average value at the inlet, while average static pressure  $P_g^2$  was specified at the outlet boundary. Here, the inlet total pressure and total temperature were set to 5529.3 Pa and 216.65 K, respectively. The different points on the compression performance map were obtained by providing a series of outlet static pressure values that gradually increased until the working point reached the near-stall region where the simulation could not achieve convergence. A mixing plane approach was imposed at the rotor/stator interface. The pitchwise boundaries were connected by periodic conditions. On the blade surfaces and the endwalls, nonslip

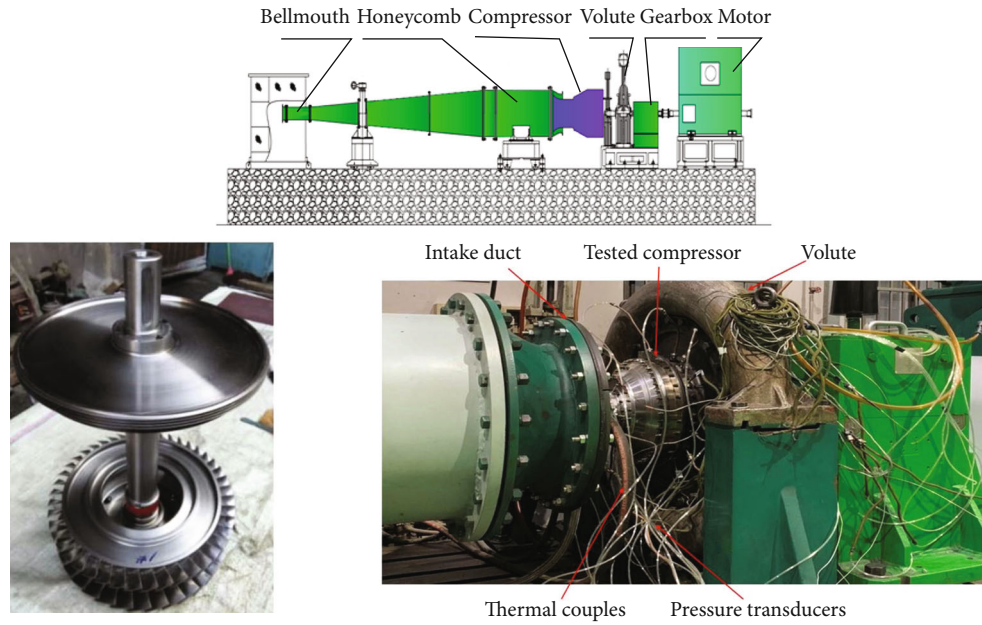


FIGURE 5: Sketch of the test rig, compressor, and rotor.

adiabatic conditions were applied. The designed rotation speed of this compressor was 25000 rpm, and the corrected rotation speed for all calculations was 100% of the design speed.

**2.2.3. Turbulence, Transition, and Wall Modeling.** Figure 4 compares the compressor characteristic curves calculated by different turbulence models. In this study, the SST  $k-\omega$  turbulence model with or without transition model, the  $k-\epsilon$  turbulence model, and then standard  $k-\omega$  turbulence model, as incorporated within the CFX code, were used as the numerical verification models for predicting the fully turbulent flow. It can be found that the total pressure ratio of the SST turbulence model with transition model was in the best agreement with the experimental results, while that of the other three turbulence models was somewhat higher than the experimental results, which was more obvious close to the blocking flow. In the efficiency characteristic diagram, the calculation results of all the turbulence models differed a little from each other and coincided with the experimental values. There was only some deviation in the near blocking condition, but the error was within the allowable range. In contrast, the computed results of SST turbulence model with transition model were in the best accordance with the test results.

The SST  $k-\omega$  model was proposed by Menter et al. [25], and the core idea was that the robustness of the  $k-\omega$  model was used near the wall to capture the flow at the viscous bottom, while the standard  $k-\epsilon$  model was used in the mainstream region to avoid the disadvantage of the  $k-\omega$  model that was too sensitive to the inlet turbulent parameters. Meanwhile, the turbulent viscosity was redefined to consider the turbulent shear stress transport. The advantages of the  $k-\omega$  model for the near wall region and standard  $k-\epsilon$  model for the far-field area were integrated.

TABLE 3: Roughness magnitudes on the rotor blade surfaces.

Case number	$k^+$	$R_a$ ( $\mu\text{m}$ )	Rough regime
1	0	0	Aerodynamically smooth regime
2	1.0	5.6	
3	3.3	16.1	
4	7.3	32.4	Transitionally rough regime
5	20.8	80.6	
6	35.9	129.0	
7	46.6	161.3	
8	57.7	193.5	
9	75.1	241.9	Fully rough regime
10	105.6	322.6	
11	137.8	403.2	
12	171.4	483.9	

The transition process of laminar-turbulent played an important role in the calculation and prediction of turbomachinery at low Reynolds number, including the formation location of the separation and transition and their effects on the compressor aerodynamic performance. In this paper, the SST  $k-\omega$  turbulence model coupled with the  $\gamma-\theta$  transition model was employed in computations after model correction [26] and numerical validation to capture the laminar boundary layer separation and transition phenomenon on the blade surface and to study the influence of surface roughness on aerodynamic performance of the compressor at low Re.

Automatic rough wall processing for the turbulence model method was used in this study, which could automatically convert from a wall function to the low-Re near-wall formula, allowing for highly accurate simulations at the

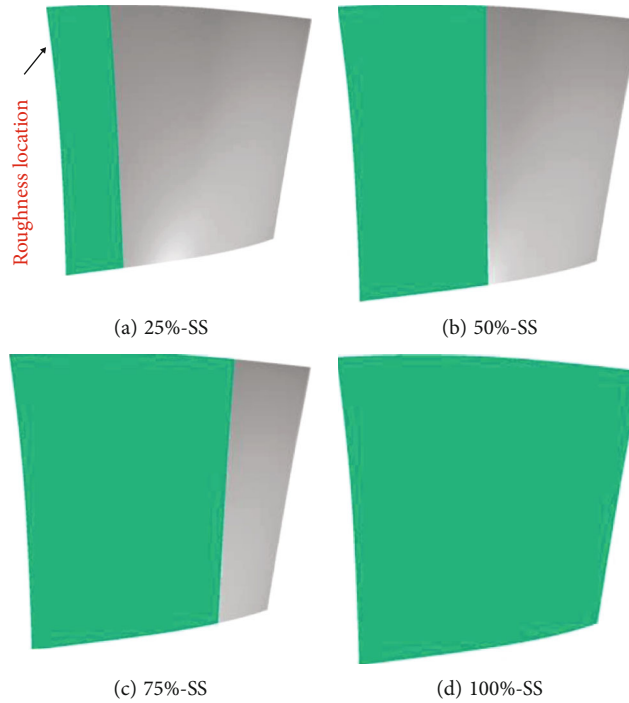


FIGURE 6: Roughness locations on the suction side of the rotor.

sublayer portions of the boundary layer. Moreover, this wall treatment method has been extended to rough walls. The transition momentum thickness Reynolds number in the  $\gamma$ - $\theta$  model was modified to simulate the effects of roughness by combining automatic near-wall processing with the transition model.

**2.2.4. Experimental Rigs and Test.** The experiment was conducted on the compressor test bench of the Institute of Engineering Thermophysics, Chinese Academy of Sciences. The compressor was driven by an 800 kW AC motor with a rated rotation speed of about 3000 rpm, and they were connected by a gearbox with a transmission ratio of 1 : 12. The flow rate was measured by the flow pipe installed in the intake duct, and the stall margins were detected by five high-frequency dynamic pressure sensors (Kulite XCQ-062), which were distributed equally along the casing wall in front of the rotor. The performance parameters and characteristic curves were obtained by measuring the total pressure and total temperature at the inlet and outlet of the compressor [24]. A schematic diagram of the rig, compressor, and rotor is shown in Figure 5.

In general, the results showed that the predicted performance parameters were basically in good agreement with the test results, and the error of the numerical simulation was within the allowable range. Therefore, the numerical method was reliable and could be used for further investigations.

### 2.3. Roughness Magnitudes and Locations

**2.3.1. Roughness Magnitudes.** Previous studies have shown that the laminar flow separation zone may increase signifi-

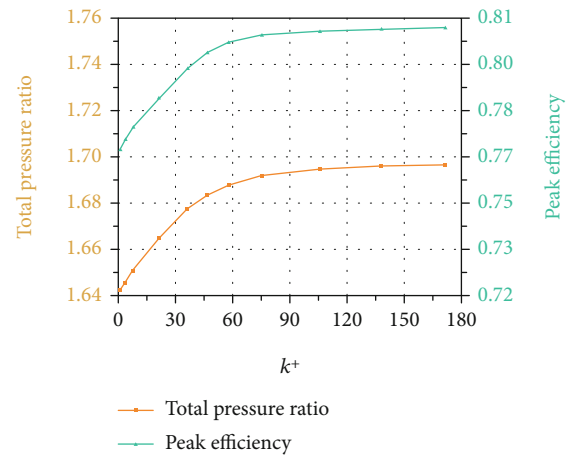


FIGURE 7: Variations of the aerodynamic performance parameter with increasing  $k^+$ .

cantly, even reaching 60% of the blade length, at low Reynolds numbers ( $Re < 105$ ). Under such conditions, roughness could obviously affect the flow separation and transition, thus influencing the aerodynamic characteristics of the compressor.

Roughness usually refers to the geometric roughness of a processed or contaminated surface and is expressed by the geometric roughness  $R_a$ , while fluid mechanics is generally described by equivalent sand roughness  $k_s$ . Koch and Smith [27] pointed out that the wall friction coefficient  $C_f$  can be calculated from  $k_s$  (see Equation (1)) that the roughness Reynolds number  $k^+$  can be expressed as a function of  $Re$ ,  $C_f$ , and  $k_s$  (see Equation (2)) and that  $k_s$  and  $R_a$  satisfy the

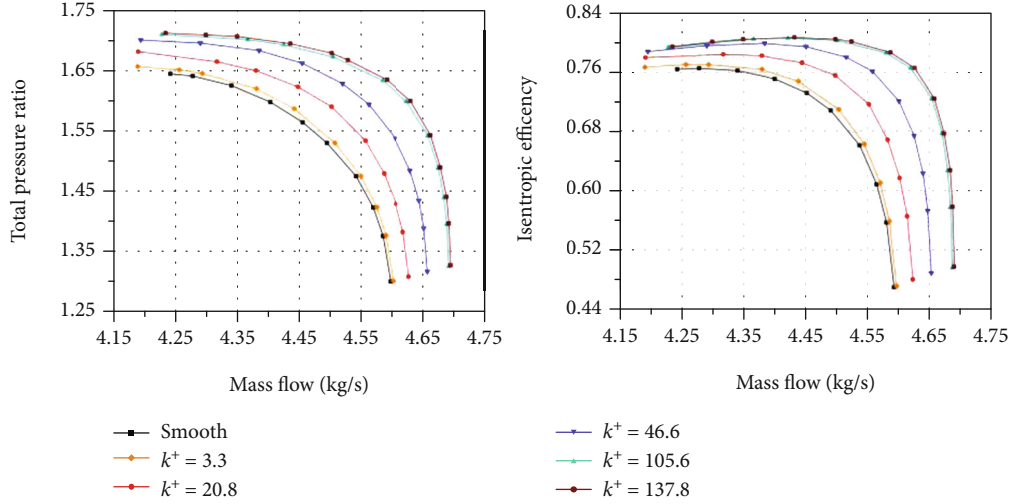


FIGURE 8: Influences of surface roughness on the aerodynamic performance of the compressor.

relationship given in Equation (3).

$$C_f = \left( 2.87 + 1.58 \lg \frac{C}{k_s} \right)^{2.5}, \quad (1)$$

$$k^+ = \text{Re} \frac{k_s}{C} \sqrt{\frac{C_f}{2}}, \quad (2)$$

where

$$k_s = 6.2R_a. \quad (3)$$

In addition, the Reynolds number is defined by  $u$ ,  $C_x$ ,  $\rho$ , and  $\mu$  (see Equation (4)) in this paper, where  $u$  is the rotor tip inlet velocity,  $C_x$  is the chord length of the rotor tip, and  $\rho$  and  $\mu$  are the rotor inlet density and viscosity, respectively. To ensure the similar working conditions of the compressor under different Reynolds numbers, numerical simulation is carried out at the same corrected rotating speed and the same corrected mass flow. Table 2 shows the specific parameters of the research.

$$\text{Re} = \frac{\rho u C_x}{\mu}. \quad (4)$$

The roughness Reynolds number  $k^+$  is a useful criterion for dividing the roughness range. For a  $k^+ < 5$ , the viscous sublayer is fully established (aerodynamically smooth regime), while for  $5 < k^+ < 70$ , the roughness elements are slightly thicker than the viscous sublayer and start to disturb it (transitionally rough regime). As  $k^+$  exceeds 70, the sublayer is destroyed and viscous effects become negligible (Fully rough regime) [1]. To effectively stimulate the transition, considering the delay of the transition at the compressor blade surface and the large laminar flow area under low-Re conditions, a total of 12 roughness levels ranging from  $k^+ = 1.5$  to  $k^+ = 171.4$  were

TABLE 4: Predicted performance parameter of the compressor at typical roughness magnitudes.

Roughness magnitudes.	Choked mass flow (kg·s <sup>-1</sup> )	Peak efficiency	Total pressure ratio
Smooth	4.5966	0.76517	1.6409
$k^+ = 3.3$	4.6009	0.77051	1.6456
$k^+ = 20.8$	4.6272	0.78411	1.6648
$k^+ = 46.6$	4.6571	0.79892	1.6834
$k^+ = 105.6$	4.6910	0.80593	1.6928
$k^+ = 137.8$	4.6945	0.80605	1.6941

set, which covered as many roughness magnitudes as possible to explore the influences of blade roughness on the aerodynamic performance of small-scale compressors. The geometric roughness  $R_a$  and the dimensionless roughness parameter  $k^+$  corresponding to these 12 roughness magnitudes are shown in Table 3.

**2.3.2. Roughness Locations.** As mentioned above, Morini et al.'s [18] research showed that the effects of the surface roughness on the rotor were greater than those on the stator, and the suction surface had a greater influence on performance than the pressure surface. Therefore, the roughness on all blade surfaces of the rotor (labeled ALL) was first set to observe the variations in performance. Then, roughness was added at different locations on the suction surface of the rotor to explore the most effective location. Four roughness locations were imposed on the suction surface covering 25%, 50%, 75%, and 100% of the suction side from the leading edge (marked 25%-SS, 50%-SS, 75%-SS, and 100%-SS, as shown in Figure 6).

Furthermore, from the above 12 roughness schemes, six typical roughness schemes including  $k^+ = 0$ ,  $k^+ = 3.3$ ,  $k^+ = 20.8$ ,  $k^+ = 46.6$ ,  $k^+ = 105.6$ , and  $k^+ = 137.8$  were selected from the ALL scheme including all the three regions to represent

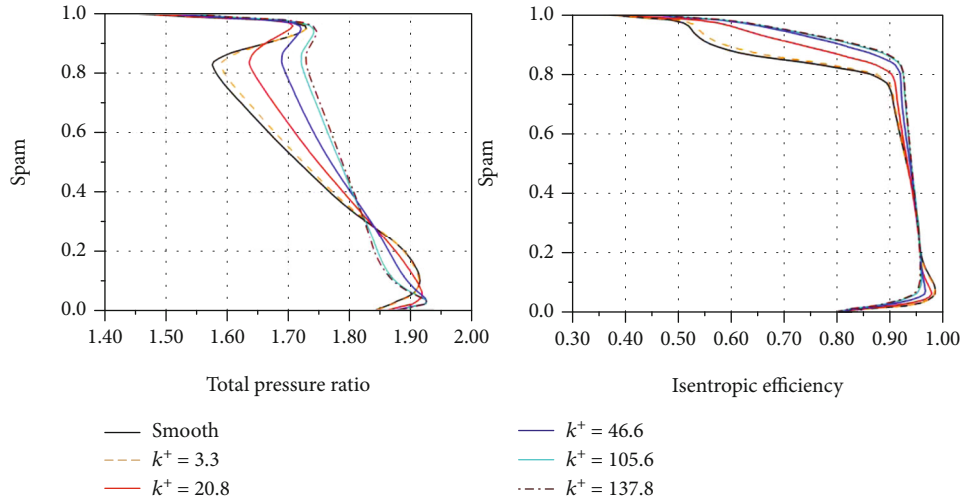


FIGURE 9: Spanwise variation of performance parameters at the compressor rotor outlet section.

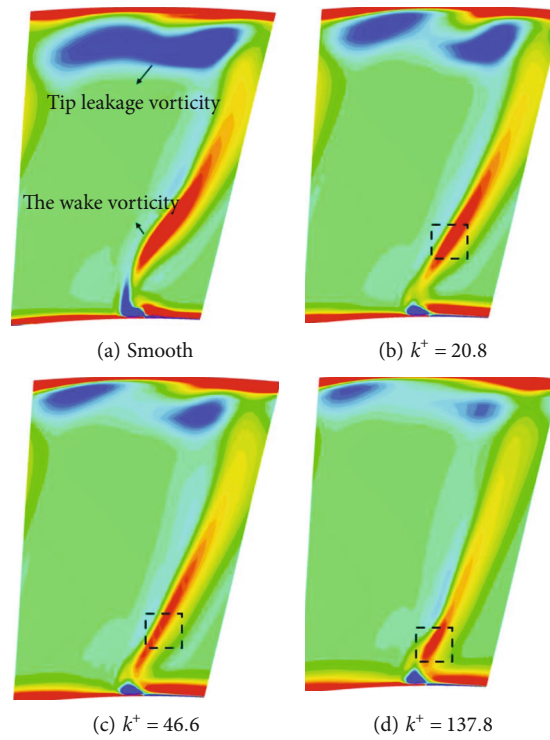


FIGURE 10: Distribution of streamwise vorticity on rotor outlet plane at different  $k^+$ .

the flow characteristics within the different region for further analyses.

### 3. Results and Discussion

#### 3.1. Effects of Roughness Magnitudes on the Aerodynamic Performance

3.1.1. Overall Trends in Aerodynamic Performance. The rotor blade surface roughness would considerably affect the aerodynamic performance of the compressor under low-Reynolds number conditions. Figure 7 shows the variation

of compressor peak efficiency and corresponding total pressure ratio at the design point with the increase of dimensionless roughness parameter  $k^+$ . The result showed that the peak efficiency and the total pressure ratio of the compressor first raised rapidly with the increase of  $k^+$ ; then, the increase in performance parameters gradually slowed down after  $k^+ = 80$ . Finally, both values of them reached the maximum and tended to be stable.

Figure 8 shows the characteristic curves of the compressor for the six cases selected from the ALL scheme. The variation trends for the total pressure ratio and isentropic efficiency were similar to the six roughness magnitudes.

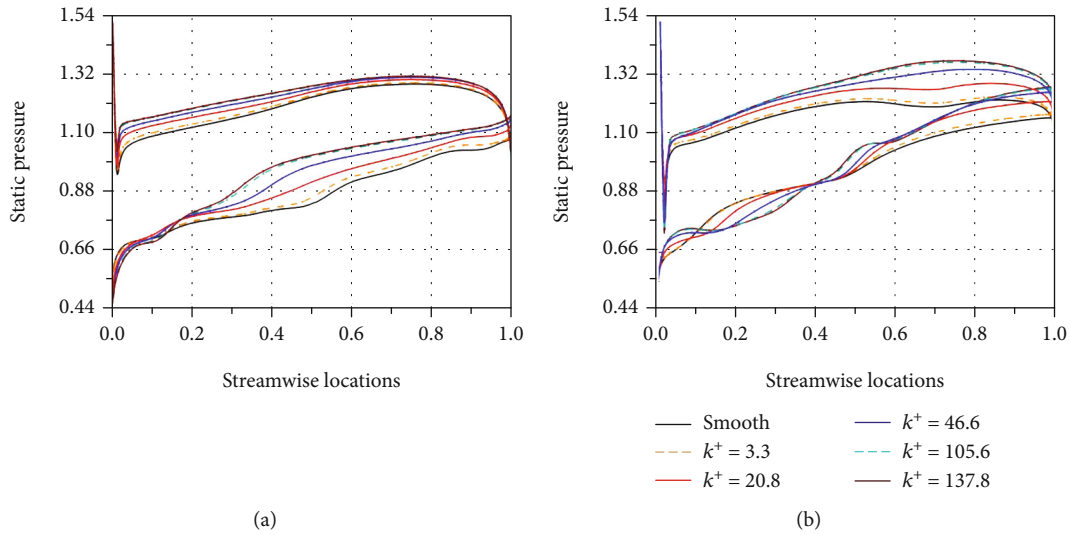


FIGURE 11: Blade loading distribution at 10% and 90% span heights.

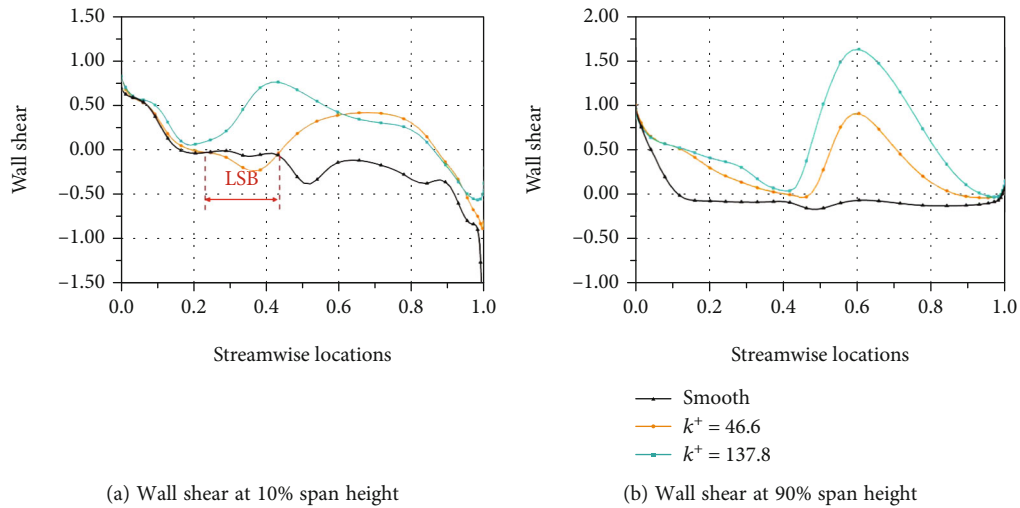


FIGURE 12: Skin normalized wall shear of the suction side at  $k^+ = 46.6$  and  $137.8$ .

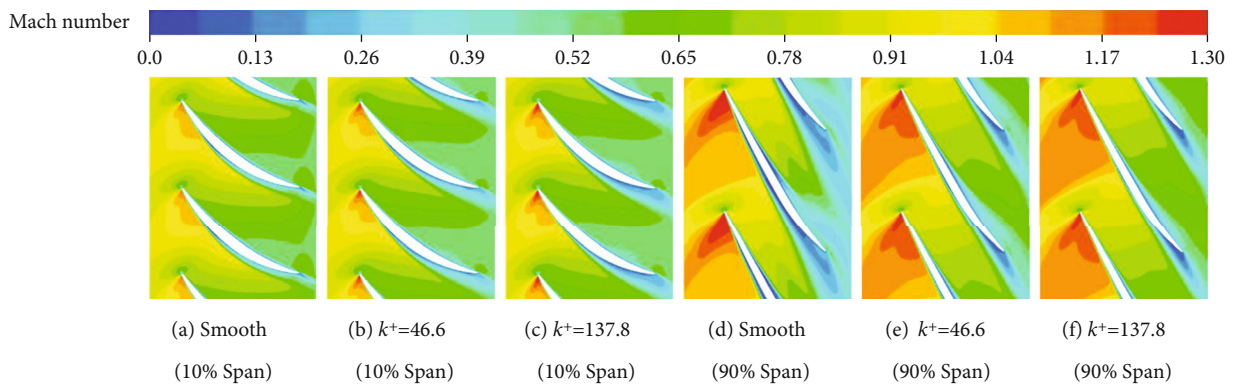


FIGURE 13: Relative Mach number contour versus  $k^+$  at different span locations.

However, roughness caused the curve to shift to the upper right, and the degree of deviation increased with the increase of  $k^+$ . It can be noticed that the impact of roughness on the aerodynamic performance of the compressor was reflected

in the increase of total pressure ratio and isentropic efficiency on the one hand and in the change of overall flow rate on the other hand. The maximum increase in total pressure ratio, peak efficiency, and choked mass flow were

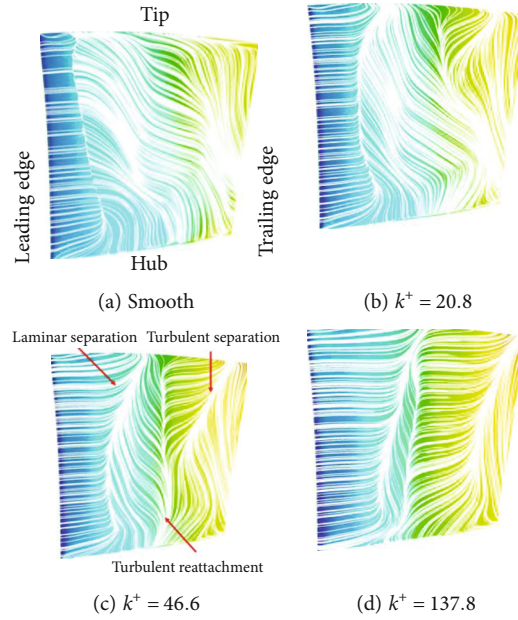


FIGURE 14: Limiting streamline on the rotor suction surface at different  $k^+$ .

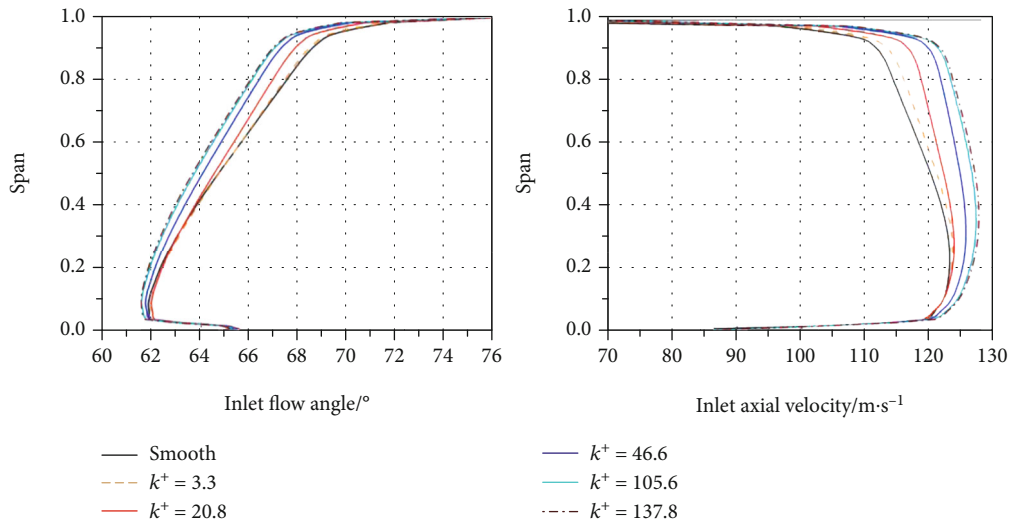


FIGURE 15: The spanwise distributions of the inlet parameters for the rotor at different  $k^+$ .

approximately 4.01%, 5.34%, and 2.24%, respectively, at  $k^+ = 137.8$ . Table 4 presents the concrete performance parameters for the six cases. The compressor efficiency and pressure ratio were more sensitive to blade surface roughness compared with the choked mass flow. In addition, roughness increased the compressor surge margin to some extent, and the choked mass flow increased more than the near stall flow. In fact, the surface roughness at low Re can effectively restrain the boundary layer from growing rapidly after the transition, thus reducing the blocking and mixing loss of blade trailing edge. Furthermore, the compressor overall mass flow increased, and the steady work range was broadened [28].

Figure 9 reports the radial profiles of the mass-averaged stage total pressure ratio and isentropic efficiency at the rotor outlet section for the six cases. With increasing  $k^+$ ,

the total pressure ratio slightly decreased at 5%~30% span and significantly increased at 30%~90% span. Moreover, the increasing degree of parameters was significantly greater than the decreasing degree. At  $k^+ = 137.8$ , the total pressure ratio at the blade root reduced approximately 3.67%, while it increased about 9.49% at the blade tip. The variation trend in the spanwise isentropic efficiency was similar to that of the total pressure ratio. Roughness somewhat reduced the efficiency of the blade root while dramatically improving the blade tip efficiency until both values almost remained constant. In addition, the efficiency of the main flow field of the cascade channel was significantly higher than that near the endwall due to the loss of the endwall.

In order to preliminarily discuss the flow mechanisms along the spanwise distribution of the aerodynamic performance at the rotor outlet, Figure 10 shows the streamwise

vorticity distribution on rotor outlet plane. For the smooth blade, there were extremely large vorticity regions caused by tip leakage which were identified near blade tip regions, while there was also a region near the blade root with a strong axial component of vorticity due to the wake shedding. As  $k^+$  increased, the range and intensity of the leakage vorticity near the rotor blade tip decreased significantly, reaching the minimum at  $k^+ = 137.8$ , and the intensity of the shed wake vorticity from the middle span to the top span also decreased to a certain extent. In addition, the starting position of the wake vorticity (the black square part in the figure) gradually moved down to the blade root, reaching the bottom (about 20% of the blade height) at  $k^+ = 137.8$ . Therefore, with the increase of  $k^+$ , the loss caused by the streamwise vorticity from the middle to the top of the blade continuously decreased, while it near the blade root slightly increased, which together led to the change of compressor performance. Certainly, the result was consistent with the performance curve in Figure 9.

**3.1.2. Blade Loading and Wall Shear Stress of the Rotor Suction Surface.** The influence of rotor surface roughness on blade loading is shown in Figure 11 with different spanwise heights (10% span and 90% span). The static pressure along the  $y$ -axis was nondimensionalized by the reference pressure (inlet total pressure, i.e., 5529.3 Pa). In Figure 11(a), the overall static pressure distribution of the pressure surface (PS) changed a little. As  $k^+$  increased, the acceleration zone of the suction surface leading edge (10%-30%  $C_x$ ) and the middle section (45%-55%  $C_x$ ) gradually disappeared, resulting in a decrease in momentum of main flow and an increase in flow loss. In addition, the transition occurred earlier with increasing roughness. The overall blade loading of the suction surface decreased from the middle section to the trailing edge, and the zone of the pressure envelope also decreased. The performance ability of the blade root decreased. Figure 11(b) shows that both the PS and SS loading significantly changed at 90% span. The static pressure of the PS increased, and the deceleration section downstream of the SS leading edge shock wave (10%-40%  $C_x$ ) gradually transformed into an acceleration section. The momentum of the main flow increased after acceleration, and the ability to resist the reverse pressure gradient was also enhanced, so the laminar flow separation loss was effectively suppressed. Furthermore, the zone of the pressure envelope increased, which meant the performance ability of the blade tip was enhanced. In addition, due to the increase of radial pressure gradient, the radial migration of the fluid toward the blade tip was more difficult. As seen at  $k^+ = 46.6$ , laminar separation and turbulent reattachment occurred on the suction surface at 45%  $C_x$  from the leading edge; that is to say, there was a laminar separation bubble (LSB) that accounted for approximately 15% of the suction surface from the leading edge, and the area where the LSB was located presented a “platform” distribution. And the blade loading changed little as  $k^+$  increased from 105.6 to 137.8.

The skin friction coefficient for the rotor SS is given in Figure 12. For the smooth blade, the laminar flow separation

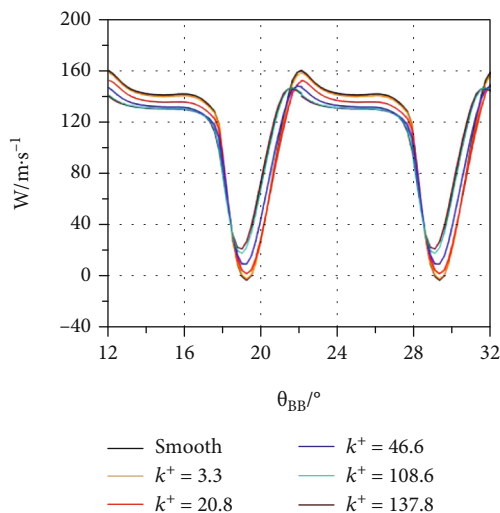


FIGURE 16: The wake velocities of the rotor at 50% span height at different  $k^+$ .

zone and the flow loss were large. As the blade surface was roughened with  $k^+ = 46.6$ , the laminar separation of the blade tip was effectively inhibited, and the length of LSB was approximately 10% of axial chord length, while the LSB was approximately 25% of the axial chord length at the blade root. As  $k^+$  increased to 137.8, there was no LSB on the rotor SS at both the blade root and tip. In general, the figure shows that with  $k^+$  increasing, the LSB at the root and tip of the blade was gradually suppressed or even eliminated, and the wall shear stress would rise to a high level.

Figure 13 illustrates the relative Mach number contours of the flow field. At the blade root (10% span), because the flow velocity of the main stream was small, the stronger viscous dissipation in the turbulent region caused by roughness was dominant. Therefore, the boundary layer continued to accumulate and develop under the action of friction. This led to significant thickening of the boundary layer at the trailing edge (as seen in Figure 13(c)), which meant the mixing loss and flow blockage were intensified. In contrast, at the blade tip (90% span), due to high speed of the main stream, the effect of roughness to restrain laminar flow separation was dominant. The development of the boundary layer was effectively restricted and the width and depth of the wake continued to decrease.

**3.1.3. Streamlines of the Rotor Suction Surface.** Figure 14 shows the rotor SS streamlines for the four typical cases (Smooth,  $k^+ = 20.8$ ,  $k^+ = 46.6$ , and  $k^+ = 137.8$ ). Compared with the smooth case, the laminar flow separation from the tip to the middle of the blade was delayed as the blade was roughened, and the transition began sooner. As seen in Figure 14(c), turbulent reattachment and turbulent separation occurred after the transition, and the overall separation zone greatly reduced. At  $k^+ = 20.8$ , the laminar separation point moved downstream approximately 4.1%  $C_x$  and reattached on the wall at about 36.5%  $C_x$  downstream of the separation line. With  $k^+$  increasing to 46.6,

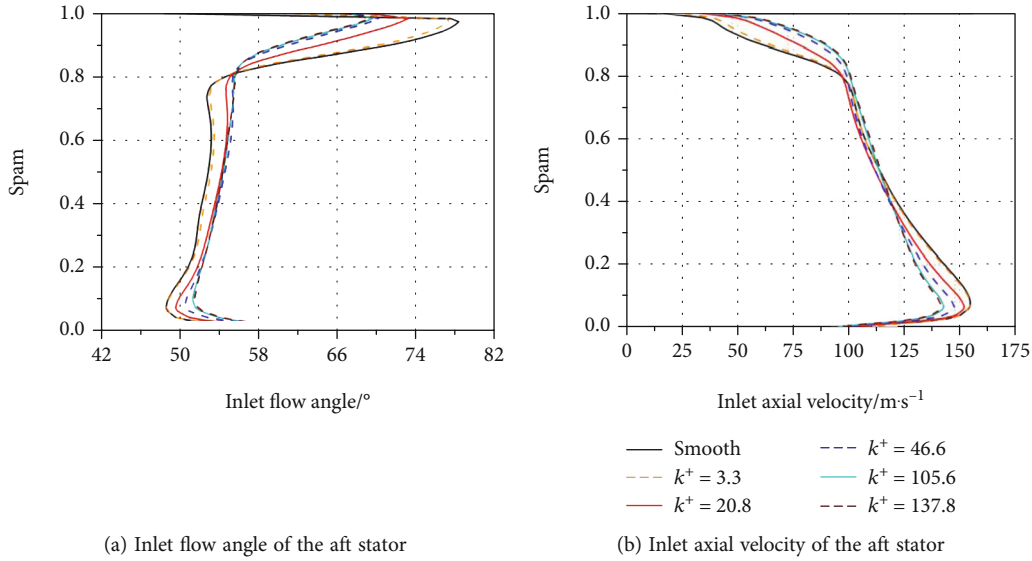


FIGURE 17: The span distribution of the inlet parameters for the aft stator at different  $k^+$ .

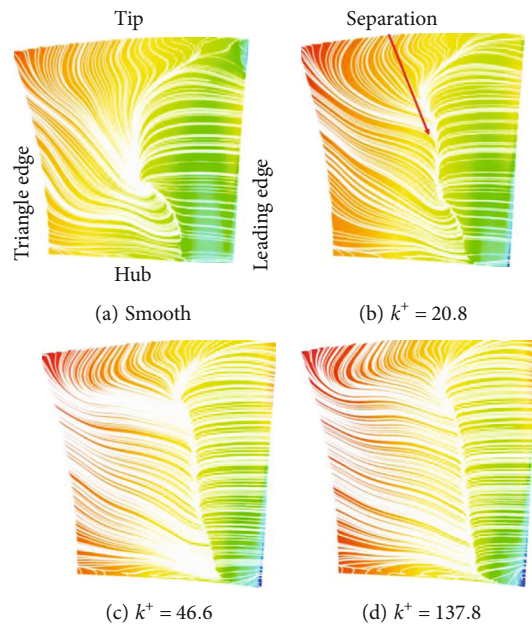


FIGURE 18: Limiting streamline on stator suction surface at different  $k^+$ .

the laminar separation point continued to move downstream, and the LSB shortened by approximately 10.2%  $C_x$ . Turbulent separation appeared at the trailing edge. As  $k^+$  increased to 137.8, roughness greatly suppressed the development of the LSB, of which the length and maximum thickness decreased significantly and the turbulent separation zone at the trailing edge nearly disappeared. In general, roughness delayed laminar flow separation, promoted the transition to occur in advance, and accelerated turbulent reattachment, which reduced the separation loss and improved the aerodynamic performance of the compressor to a large extent.

3.1.4. *Inlet and Outlet Flow Conditions of the Rotor.* The roughness of rotor blade surface resulted in the change of the mass flow rate inside the compressor, which changed the rotor inlet and outlet flow conditions. Figure 15 shows variations in the inlet condition of the rotor (under the same outlet back pressure). With the increase of roughness, the inlet angle decreased, the angle of attack also decreased, and the rotor spanwise inlet axial velocity increased. Therefore, the ability of the fluid in the blade boundary layer to overcome the viscous momentum and resist the reverse pressure gradient was enhanced, resulting in a decrease of low-energy fluid. In other words, the flow field around the

rotor area was optimized, and the compressor efficiency was improved. In addition, these changes subsequently influenced the blade loading and the wall shear stress of the rotor.

In Figure 16, the relative velocity  $W$  downstream the rotor at 50% span was plotted against the blade-to-blade angle position  $\theta_{BB}$  for the six cases analyzed. With increasing roughness, no obvious shift of the center of wake toward either the pressure or the suction side can be noticed, but the mass flow area of the channel decreased due to fluid dynamic blockage. Furthermore, the velocity magnitude at the potential wake core increased. This led to a decrease in the width and depth of the wake, which reached the minimum at  $k^+ = 137.8$ . Meanwhile, the compressor aerodynamic performance achieved the best.

### 3.1.5. Inlet Flow Conditions and Streamlines of the Aft Stator.

Figure 17 reports the change trend of the spanwise inlet flow angle and axial velocity of the aft stator at different  $k^+$ . As shown in Figure 17(a), the inlet flow angle at 5%-80% span increased a little; that is to say, the attack angle and flow turning angle increased. Therefore, the flow adverse pressure gradient was enhanced and the centrifugal force generated by the flow deflection advanced the flow separation, leading to the increase of the flow loss. However, at 80%-95% span, the inlet flow angle decreased, which optimized the flow field and improved the efficiency. In Figure 17(b), at the blade tip, the axial velocity increased; thus, the momentum of main flow increased and the flow loss decreased. At the blade root, the axial velocity decreased, which made the corner separation more likely to occur. Generally, it was difficult to distinguish which part of blade root and blade tip was dominant, so further analysis was required.

Figure 18 presents the stator suction surface streamlines for the typical four cases. With the increase of  $k^+$ , the position of the overall separation of the stator suction surface gradually advanced, and the corner separation further intensified. In other words, the roughness of rotor blade surface increased the flow loss of the aft stator and aggravated the incoordination between stages, which limited further improvement of the overall aerodynamic performance of the compressor.

## 3.2. Effects of Roughness Locations on the Aerodynamic Performance

**3.2.1. Overall Trend of Peak Efficiency.** In addition to the magnitudes of the surface roughness, the locations of the surface roughness also affected the separation and transition of the boundary layer on the blade surface, which then influenced the flow loss and aerodynamic characteristics of the compressor. In Figure 19, the variation in compressor peak efficiency with roughness magnitudes and locations was given. The locations of surface roughness had little effect on the peak efficiency at  $k^+ < 46.6$ . As  $k^+$  increased to 105.6, the increases in the peak efficiency of the 25%-SS and 50%-SS cases were greater than those of the 75%-SS and 100%-SS cases, and the locations of the roughness had a larger impact as  $k^+$  continued to increase. At  $k^+ = 137.8$ , the peak efficiencies of the 25%-SS and 50%-SS cases were

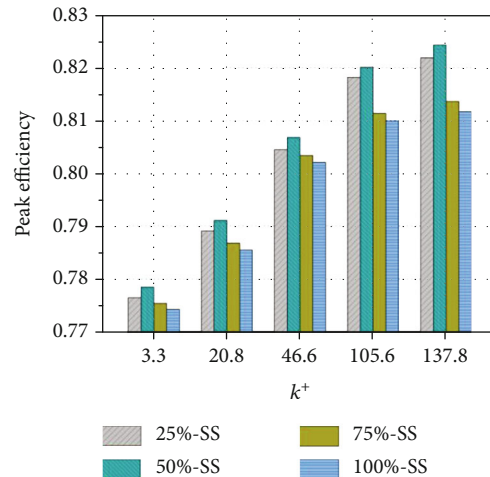


FIGURE 19: The variation in the peak efficiency with different surface roughness magnitudes and locations.

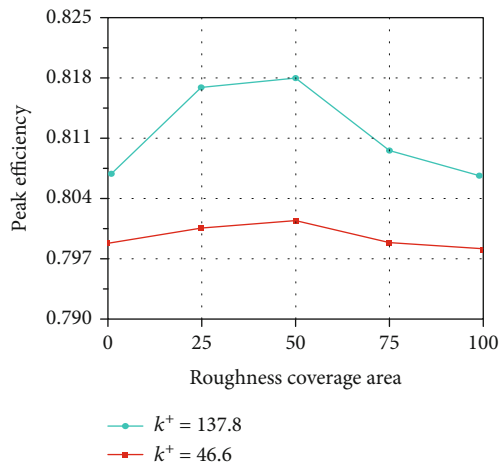


FIGURE 20: The variation in the peak efficiency with different roughness coverage area at  $k^+ = 46.6$  and  $k^+ = 137.8$ .

significantly higher than those of the 75%-SS and 100%-SS cases. Thus, two typical roughness values,  $k^+ = 46.6$  and  $k^+ = 137.8$ , were selected for further analysis. Figure 20 shows the variation in peak efficiency with different locations of roughness. The results indicated that the improvements in the value of the 25%-SS and 50%-SS cases were more significant than those of the 75%-SS and 100%-SS cases, and the differences between the four cases continued to grow with  $k^+$  increasing.

**3.2.2. Wall Shear Stress and Boundary Layer Analysis of the Rotor Suction Surface.** The skin shear stress of the rotor SS is given in Figure 21. As the surface was roughened with  $k^+ = 46.6$  (in Figures 21(a) and 21(c)), the laminar flow separation was suppressed to a certain extent for the four roughness locations, and the LSB at the blade tip was apparently smaller than that at the blade root. The results showed that 100%-SS, 75%-SS, and 50%-SS were more effective in eliminating laminar flow separation and inhibiting the

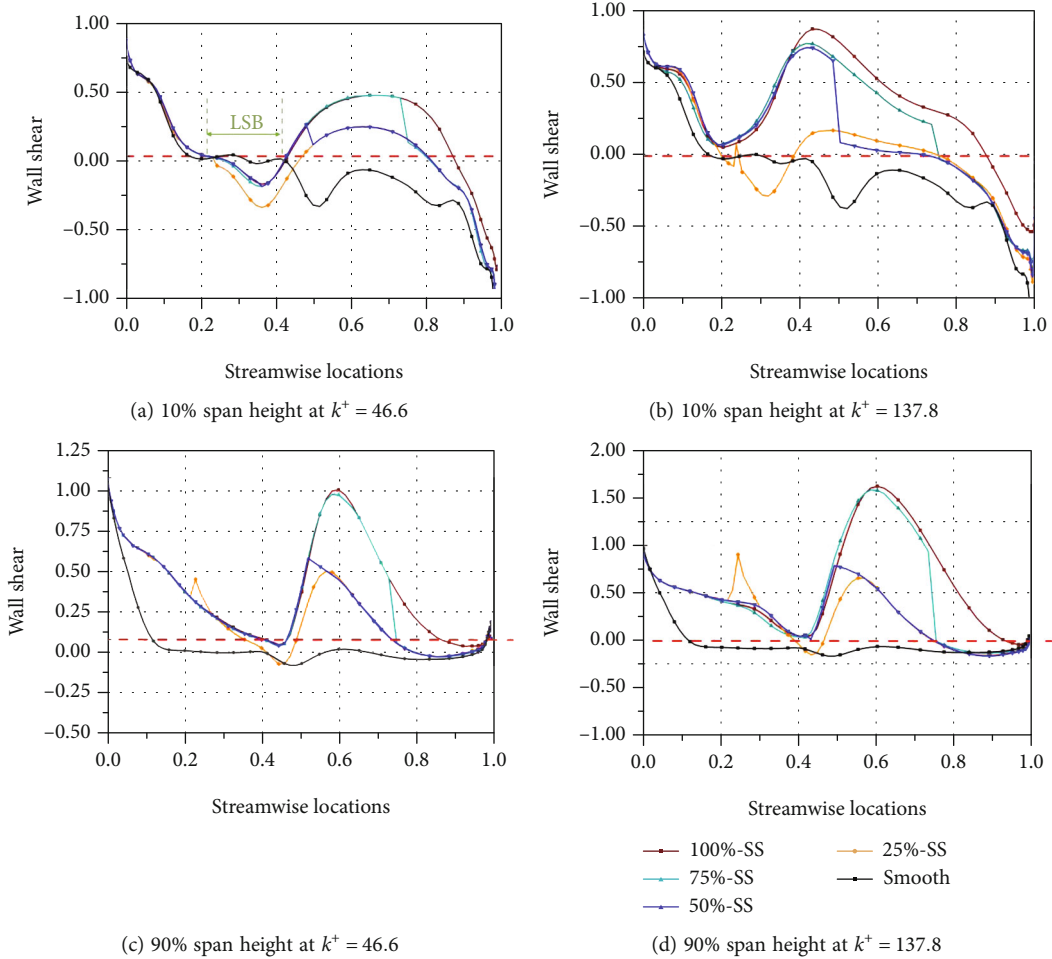


FIGURE 21: Skin wall shear distribution for the different roughness locations at  $k^+ = 46.6$  and  $137.8$ .

length of the LSB than the 25%-SS case. However, for the 100%-SS case and the 75%-SS case, the wall shear stress in the turbulent region increased to a relatively high level, enhancing the strong viscous dissipation. As a consequence, there were only slight differences in the wall shear values between the four cases under the interaction of separation loss and turbulence dissipation. In Figures 21(b) and 21(d), with  $k^+$  increasing to 137.8, the laminar separation was greatly delayed or even eliminated and the transition process was sharply accelerated, which restricted the development of the LSB. Furthermore, among the four roughness locations, only the 25%-SS case still had a significant LSB, which led to a certain separation loss. For the remaining three schemes, the 50%-SS case kept the wall shear stress at a relatively low level while eliminating the LSB. Therefore, the 50%-SS case had the most significant improvement on the aerodynamic performance of the compressor.

The blade surface boundary layer parameters at 50% span of the rotor SS are given in Figure 22. At  $k^+ = 46.6$ , surface roughness at different locations weakened laminar separation to a certain extent and inhibited the LSB's negative influence on boundary layer thickening, which alleviated the flow mixing and blocking near the rotor trailing edge

(as shown in Figure 22 (a1) and (b1)), improving the compressor peak efficiency. In Figure 22 (c1), the transition positions (the peak point of the shape factor) in 100%-SS and 75%-SS schemes were about at  $x/C_x = 0.5$ , which were a little advanced than those in 25%-SS and 50%-SS schemes of which the transition occurred nearly at  $x/C_x = 0.58$ , and the peak value of 100%-SS and 75%-SS schemes was smaller than that of 25%-SS and 50%-SS schemes. In other words, the LSB's width of 100%-SS and 75%-SS schemes was slightly less than that of 25%-SS and 50%-SS schemes, but the turbulence dissipations of them were also larger because of the higher level of wall shear stress in the turbulent region. Therefore, there was little difference in boundary layer parameters for the four different roughness locations.

Furthermore, with  $k^+$  increasing to 137.8, the development of the boundary layer was relatively more affected by the roughness locations. It can be perceived that in Figure 22 (a2) and (b2) the displacement thickness and momentum thickness of boundary layer further reduced, and the difference of the boundary layer parameters between different roughness locations became larger. Specifically, the displacement thickness and momentum thickness of the 50%-SS scheme reached the minimum, which were

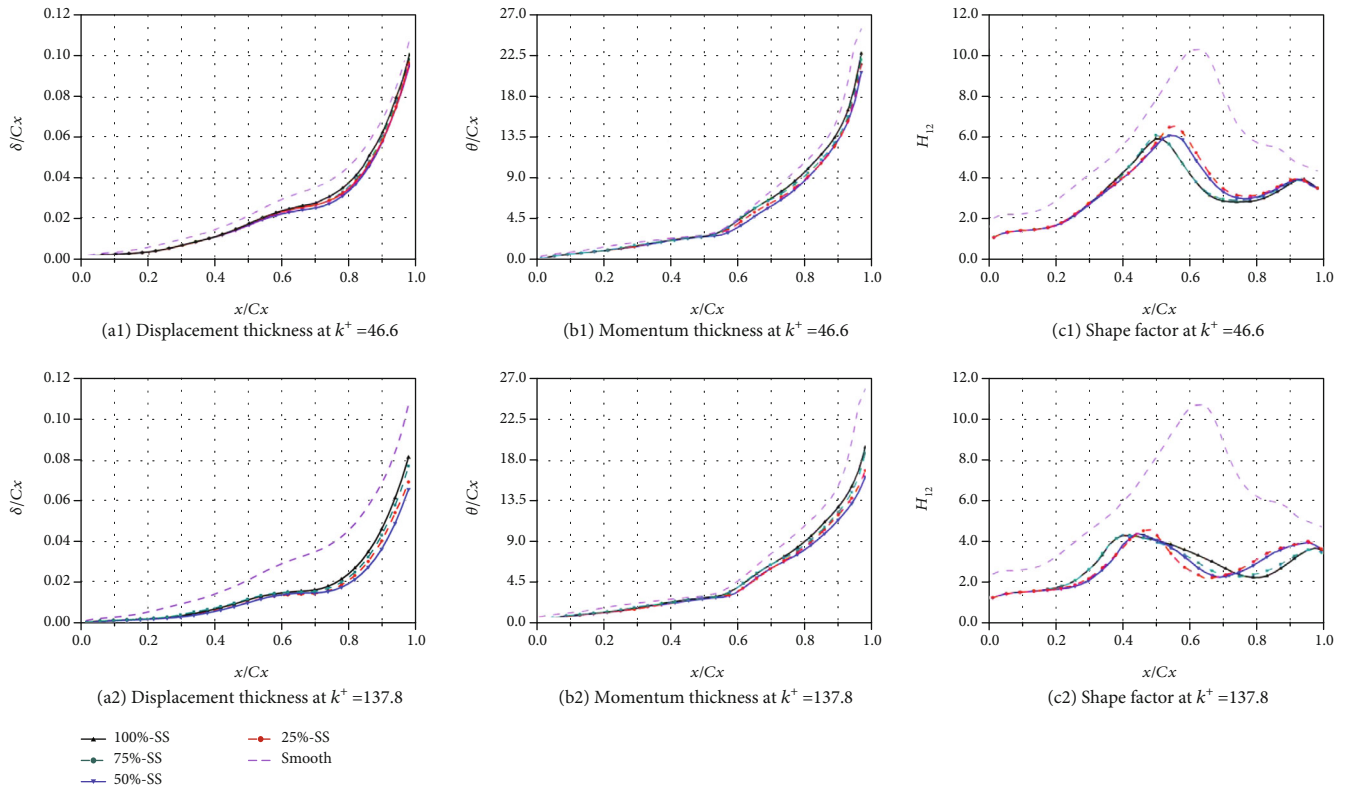


FIGURE 22: Boundary layer parameters at 50% span of the rotor suction side versus roughness locations at  $k^+ = 46.6$  and  $137.8$ .

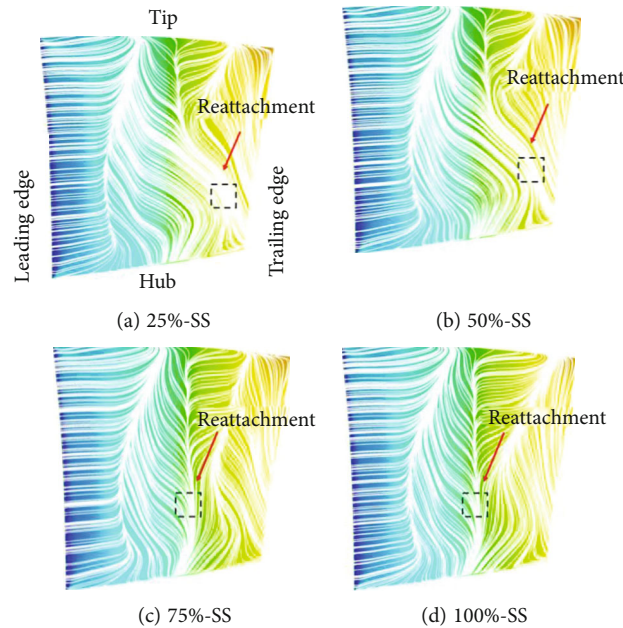


FIGURE 23: Limiting streamline on the rotor suction surface for the different roughness locations at  $k^+ = 46.6$ .

significantly smaller than that of the other three schemes. In addition, the change trend of the shape factor was similar to that at  $k^+ = 46.6$ , but the overall transition occurred earlier. In general, the 50%-SS scheme had a better balance in eliminating LSB and suppressing excessive turbulent dissipation.

3.2.3. *Streamlines of the Rotor Suction Surface.* To further clarify the influence of different roughness locations on three-dimensional separation and reattachment, Figure 23 shows the rotor SS streamlines for the four different roughness locations at  $k^+ = 46.6$ . As can be seen, the 75%-SS and

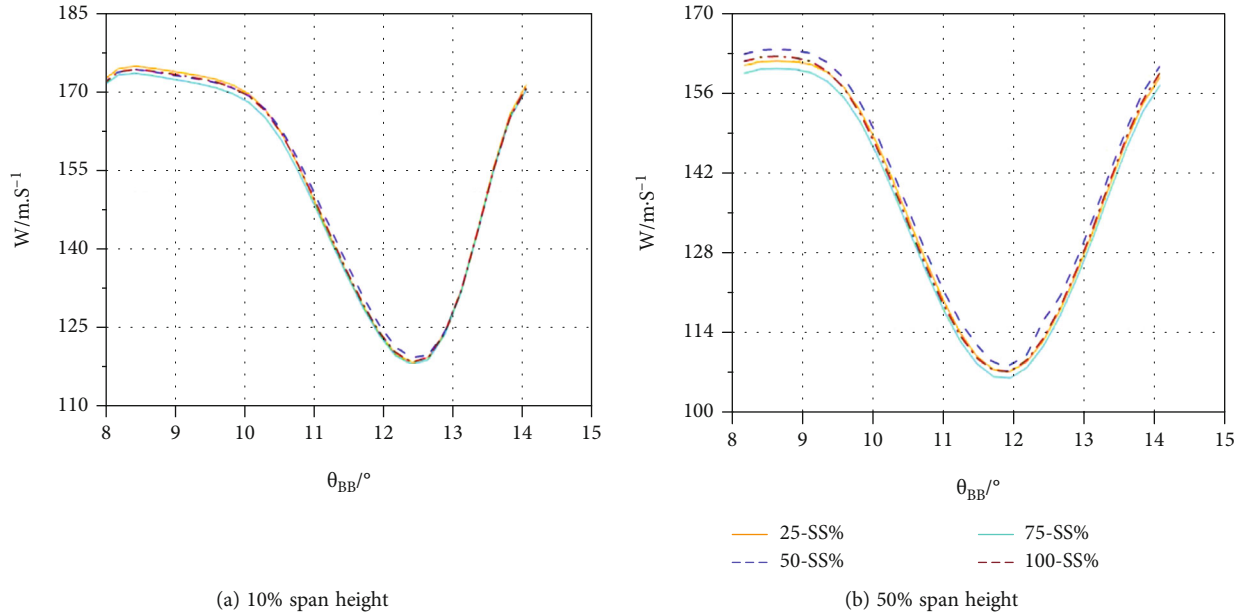


FIGURE 24: Relative velocity downstream of the stator for the different roughness locations at  $k^+ = 137.8$ .

100%-SS schemes not only better inhibited the growth and development of two-dimensional LSB but also had a significantly better effect in suppressing the three-dimensional flow separation than the 25%-SS and 50%-SS schemes. Specifically, the 75%-SS and 100%-SS schemes slightly delayed the flow separation at the blade tip and significantly promoted the transition process, so that the position of turbulence reattachment was significantly advanced, greatly inhibiting the development of the LSB and reducing the separation loss. Therefore, at  $k^+ = 46.6$ , the aerodynamic performances of the four cases are relatively close, which is also consistent with the above conclusion concerning the two-dimensional parameters.

**3.2.4. Wake Downstream the Stator.** Figure 24 presents the relative velocity,  $W$ , downstream of the stator against the blade-to-blade angle location  $\theta_{BB}$  at  $k^+ = 137.8$  for the four schemes. The profiles referred to two span heights (10% and 50%) and to a location downstream of the stator corresponding to 10% of the axial length of the stator itself from the inlet to the outlet. The results indicated that the core of the wake did not shift to the PS or the SS as the roughness locations changed, but the width and depth of the wake were the smallest for the 50%-SS case among the four cases. In addition, Back et al. [12] and Fouflias et al. [29] revealed similar results, although they showed that the center of the wake moved to the SS. They also found the phenomenon based on subsonic compressor cascades, whereas the current study referred to the transonic compressor stage. Therefore, the shift in the wake may be a characteristic of subsonic compressors [19], as this phenomenon has not been noticed in transonic compressors.

Based on the above analysis, the 50%-SS case could effectively eliminate laminar flow separation and avoid large turbulent dissipation losses in the entire roughness range for

the four roughness locations and improved the compressor performance to a large extent.

## 4. Conclusions

The surface roughness control method was effective in controlling boundary layer development and improving the compressor aerodynamic performance at low Re without imposing additional complex geometric shapes on the blade. This paper concentrated on the influences of roughness magnitudes ( $k^+$ ) and locations (25%-SS, 50%-SS, 75%-SS, and 100%-SS) on the aerodynamic performance of a small-scale 1.5-stage highly loaded transonic axial compressor under 20-km altitude conditions ( $Re = 4.5 \times 10^4$ ) by using a commercial CFD code. The main results and conclusions were summarized as follows:

- (1) The peak efficiency and the total pressure ratio of the compressor first increased rapidly with the increase of  $k^+$ , then the speed of the increase gradually slowed down after  $k^+ = 80$ . Finally, both values of them reached the maximum and tended to be stable at  $k^+ = 137.8$ . To be specific, the maximum increases in the total pressure ratio, peak efficiency, and choked mass flow were approximately 4.01%, 5.34%, and 2.24%, respectively, at  $k^+ = 137.8$ . Moreover, the steady work range of the compressor was broadened to some extent
- (2) The results showed that at low Re, the surface roughness mainly improved the stage performance by reducing the length and width of the LSB as well as the rotor tip vorticity, delaying the occurrence of three-dimensional flow separation and increasing the turbulence level near the wall. At the tip of the rotor blade, the effect of roughness to restrain or

even eliminate laminar flow separation was dominant, thus reducing separation loss and improving compressor efficiency. However, at the root of rotor blade, the advantage of LSB suppression was over-compensated by the stronger viscous dissipation and the shift of the wake core in the turbulent region. As such, the growth of the turbulent boundary layer was enhanced and the aerodynamic performance of the rotor blade root was slightly deteriorated instead. Generally, the positive effect of roughness at the blade tip was obviously greater than the negative effect of roughness at the blade root, leading to an improvement in the compressor overall performance

- (3) The locations of surface roughness had little effect on the compressor peak efficiency at  $k^+ < 46.6$ . However, with  $k^+$  increasing, the differences between the four roughness locations continued to grow. In the entire range of roughness magnitudes, the 50%-SS case can effectively keep the balance between suppressing LSB and inducing strong viscous dissipation among the four roughness location schemes. Therefore, the 50%-SS case had a better effect on improving the compressor aerodynamic performance
- (4) The roughness of rotor blade surface can dramatically improve the rotor aerodynamic performance. However, the incoordination between the subsequent stages was aggravated to a certain extent. Specifically, the flow separation of the stator was advanced and the corner separation was intensified, which limited the further improvement of the overall aerodynamic performance of the compressor. In addition, the magnitudes and locations of the surface roughness almost did not shift the center of the wake toward either the pressure or the suction side but only affected the width and depth of the wake

## Nomenclature

$C$ :	Chord length
$k_s$ :	Equivalent sand grain roughness
$k^+$ :	Nondimensional roughness height
$R_a$ :	Geometric roughness
$y^+$ :	First grid distance from the wall
$y$ :	Normal distance, Cartesian coordinate
$P_0^1$ :	Inlet total pressure
$T_0^1$ :	Inlet total temperature
$P_g^2$ :	Outlet average static pressure
$\theta_{BB}$ :	Circumferential angle
$C_f$ :	Skin friction coefficient
$C_x$ :	Axial chord length
$W$ :	Axial velocity
SS:	Suction surface
PS:	Pressure surface
RANS:	Reynolds-averaged Navier-Stokes
CFD:	Computational fluid dynamics
Ma:	Mach number
Re:	Reynolds number

LSB: Laminar separation bubble.

## Superscripts

- 1: At the inlet to the blade
- 2: At the outlet to the blade
- +: Nondimensional.

## Data Availability

The research data used to support the findings of this study are included within the article.

## Conflicts of Interest

The authors declare that they have no known competing financial interests or personal relationships that could have appeared to influence the work reported in this paper.

## Acknowledgments

The authors wish to acknowledge the financial support of the National Natural Science Foundation of China (Project No. 518366008) and the National Science and Technology Major Project of China (Project No. J2019-II-0004-0024) for this project.

## References

- [1] J. P. Bons, "A review of surface roughness effects in gas turbines," *Journal of Turbomachinery*, vol. 132, no. 2, 2010.
- [2] O. E. Balje, "A study on Reynolds number effects in turbomachines," *Journal of Engineering for Power*, vol. 86, no. 3, pp. 227–235, 1964.
- [3] H. J. Li and Z. Yang, "Separated boundary layer transition under pressure gradient in the presence of free-stream turbulence," *Physics of Fluids*, vol. 31, no. 10, p. 104106, 2019.
- [4] K. Bammert and R. Milsch, "Boundary layers on rough compressor blades," in *Turbo Expo: Power for Land, Sea, and Air. Vol. 79818*, American Society of Mechanical Engineers, 1972.
- [5] H. H. Açıkel and M. Serdar Genç, "Control of laminar separation bubble over wind turbine airfoil using partial flexibility on suction surface," *Energy*, vol. 165, pp. 176–190, 2018.
- [6] Z. Y. Cao, B. Liu, T. Zhang, X. Yang, and P. Chen, "Influence of coupled boundary layer suction and bowed blade on flow field and performance of a diffusion cascade," *Chinese Journal of Aeronautics*, vol. 30, no. 1, pp. 249–263, 2017.
- [7] R. J. Volino, "Passive flow control on low-pressure turbine airfoils," *Journal of Turbomachinery*, vol. 125, no. 4, pp. 754–764, 2003.
- [8] R. Pacciani and E. Spano, "Numerical investigation of the effect of roughness and passing wakes on LP turbine blades performance," *Turbo Expo: Power for Land, Sea, and Air*, vol. 4241, 2006.
- [9] J. P. Bons, J. Pluim, K. Gompertz, M. Bloxham, and J. P. Clark, "The application of flow control to an aft-loaded low pressure turbine cascade with unsteady wakes," *Journal of Turbomachinery*, vol. 134, no. 3, article 031009, 2012.
- [10] M. S. Genc, K. Koca, and H. H. Acikel, "Investigation of pre-stall flow control on wind turbine blade airfoil using roughness element," *Energy*, vol. 176, pp. 320–334, 2019.

- [11] S. K. Roberts and M. I. Yaras, "Effects of surface-roughness geometry on separation bubble transition," *Journal of Turbomachinery*, vol. 128, no. 2, pp. 349–356, 2006.
- [12] S. C. Back, I. C. Jeong, J. L. Sohn, and S. J. Song, "Influence of surface roughness on the performance of a compressor blade in a linear cascade experiment and modeling," *Turbo Expo: Power for Land, Sea, and Air*, vol. 48883, 2009.
- [13] D. Kong, H. Jeong, and S. J. Song, "Effects of surface roughness on evolutions of loss and deviation in a linear compressor cascade," *Journal of Mechanical Science and Technology*, vol. 31, no. 11, pp. 5329–5335, 2017.
- [14] S. A. Gbadebo, T. P. Hynes, and N. A. Cumpsty, "Influence of surface roughness on three-dimensional separation in axial compressor," *Journal of Turbomachinery*, vol. 126, no. 4, pp. 455–463, 2004.
- [15] J. H. Im, J. H. Shin, G. V. Hobson, S. J. Song, and K. T. Millsaps, "Effect of leading edge roughness and Reynolds number on compressor profile loss," *In Turbo Expo: Power for Land, Sea, and Air*, vol. 55225, 2013.
- [16] E. Syverud, O. Brekke, and L. E. Bakken, "Axial compressor deterioration caused by saltwater ingestion," *Journal of Turbomachinery*, vol. 129, no. 1, pp. 119–126, 2007.
- [17] E. Syverud and L. E. Bakken, "The impact of surface roughness on axial compressor performance deterioration," *Turbo Expo: Power for Land, Sea, and Air*, vol. 42401, 2006.
- [18] M. Morini, M. Pinelli, P. R. Spina, and M. Venturini, "Numerical analysis of the effects of nonuniform surface roughness on compressor stage performance," *Journal of Engineering for Gas Turbines and Power*, vol. 133, no. 7, article 072402, 2011.
- [19] M. Morini, M. Pinelli, P. R. Spina, and M. Venturini, "Computational fluid dynamics simulation of fouling on axial compressor stages," *Journal of Engineering for Gas Turbines and Power*, vol. 132, no. 7, article 072401, 2010.
- [20] K. Bammert and G. U. Woelk, "The influence of the blading surface roughness on the aerodynamic behavior and characteristic of an axial compressor," *Journal of Engineering for Power*, vol. 102, no. 2, pp. 283–287, 1980.
- [21] S. Chen, S. Sun, H. Xu, L. Zhang, S. Wang, and T. Zhang, "Influence of local surface roughness of a rotor blade on performance of an axial compressor stage," *In Turbo Expo: Power for Land, Sea, and Air*, vol. 55225, 2013.
- [22] S. W. Chen, C. Zhang, H. Shi, S. Wang, and Z. Wang, *Experimental research of surface roughness effects on highly-loaded compressor cascade aerodynamics*, ASME 2012- GT-68041, 2012.
- [23] M. Y. Wang, C. W. Yang, Z. Y. Li, S. Zhao, Y. Zhang, and X. Lu, "Effects of surface roughness on the aerodynamic performance of a high subsonic compressor airfoil at low Reynolds number," *Chinese Journal of Aeronautics*, vol. 8, no. 20, 2020.
- [24] C. W. Yang, X. G. Lu, Y. F. Zhang, S. Zhao, and J. Zhu, "Numerical investigation of a cantilevered compressor stator at varying clearance sizes," *Turbo Expo: Power for Land, Sea, and Air*, vol. 56635, 2015.
- [25] F. R. Menter, R. B. Langtry, S. R. Likki, Y. B. Suzen, P. G. Huang, and S. Volker, *A correlation based transition model using local variables: part I-model formulation*, ASME 2004-GT-53452, Vienna, 2004.
- [26] ANSYS CFX-Solver Theory Guide, *Release 13.0*, ANSYS, Inc, 2010.
- [27] C. Koch and L. H. Smith, "Loss sources and magnitudes in axial flow compressors," *Journal of Engineering for Gas Turbines & Power*, vol. 98, no. 3, 1976.
- [28] Z. Li and Y. Liu, "Effect of end-wall roughness on performance of transonic axial compressor," *Proceedings of the Institution of Mechanical Engineers Part G Journal of Aerospace Engineering*, vol. 231, no. 7, pp. 1213–1224, 2017.
- [29] D. Fouflias, A. Gannan, K. Ramsden, and P. Pilidis, *CFD predictions of cascade pressure losses due to compressor fouling*, ASME 2009-GT-59158, 2009.